Electronic Supplementary Material (ESI) for Physical Chemistry Chemical Physics.

Substantial enhancement of energy storage capability in polymer nanocomposites by encapsulation of $BaTiO_3$ NWs with variable shell thickness

Guanyao Wang,[a] Yanhui Huang,[b] Yuxin Wang,[a] Pingkai Jiang,[a] and Xingyi Huang*[a]

[a]Department of Polymer Science and Engineering, Shanghai Key Laboratory of Electrical Insulation and Thermal Aging, Shanghai Jiao Tong University, Shanghai 200240, China

[b]Department of Materials Science and Engineering, Rensselaer Polytechnic Institute, Troy, New York 12180, United States

*Email: xyhuang@sjtu.edu.cn

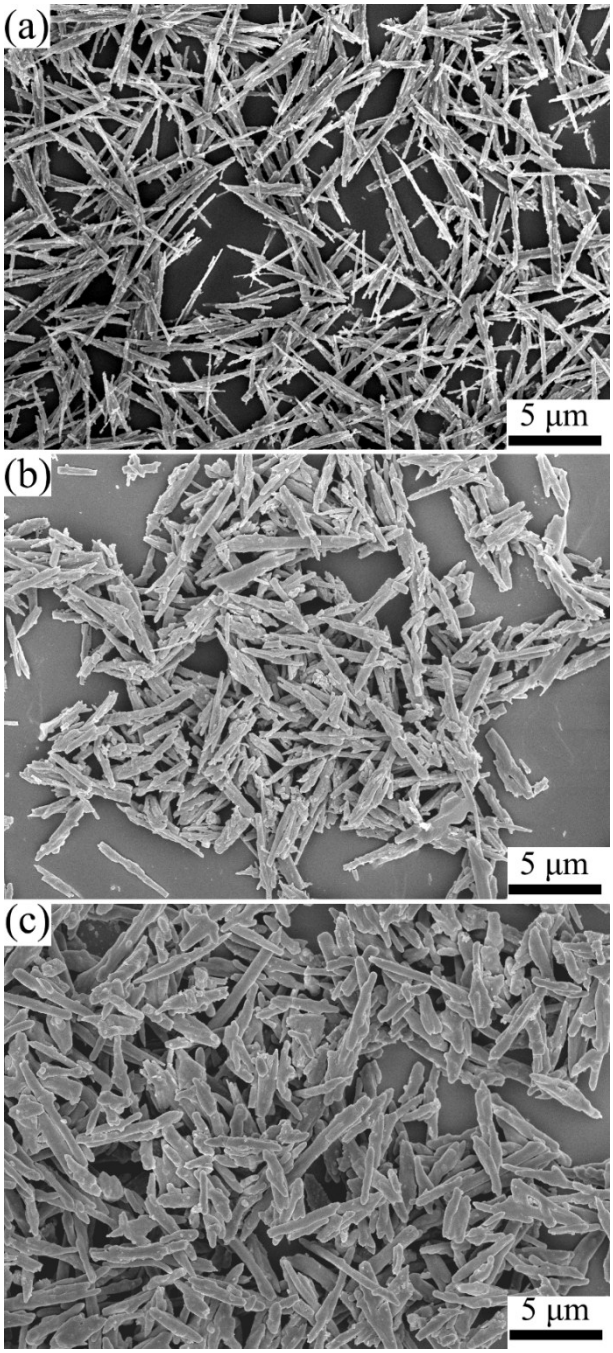

Fig. S1 SEM images of (a) raw $BaTiO_3$, (b) $mTiO_2$@$BaTiO_3$-1, and (c) $mTiO_2$@$BaTiO_3$-2 NWs after calcination.

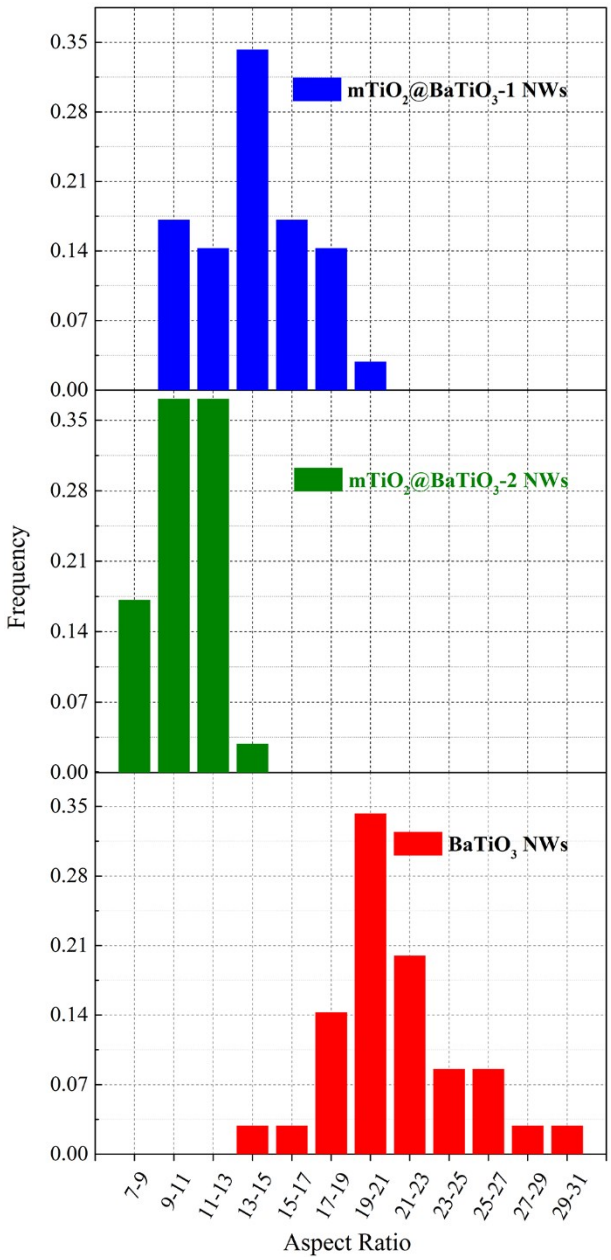

Fig. S2 The aspect ratio distribution of $mTiO_2$@$BaTiO_3$-1, $mTiO_2$@$BaTiO_3$-2 NWs and raw $BaTiO_3$ NWs.

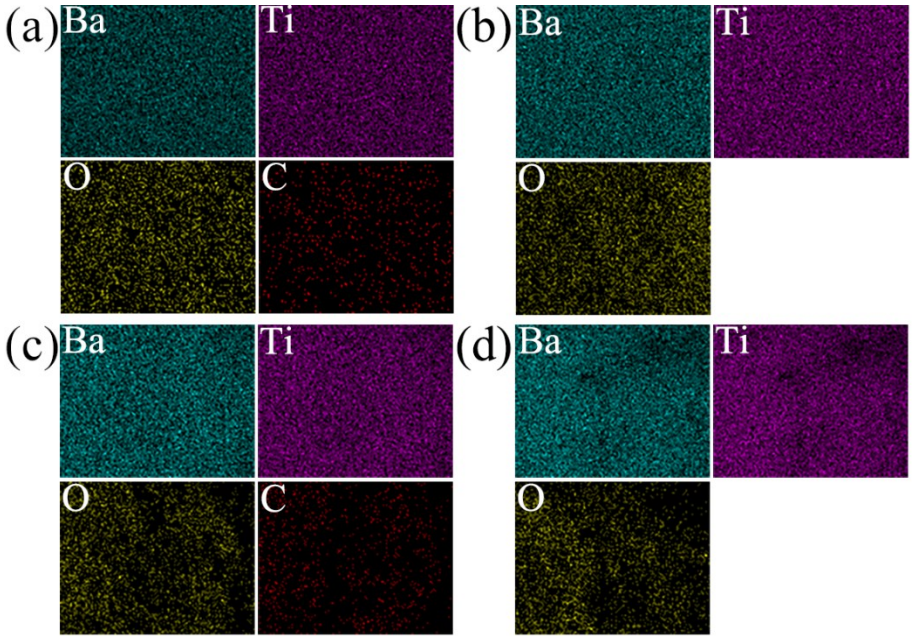

Fig. S3 The EDX elemental mapping images of $mTiO_2$@$BaTiO_3$-1 NWs (a) before and (b) after calcination. The EDX elemental mapping images of $mTiO_2$@$BaTiO_3$-2 NWs (c) before and (d) after calcination. Ba mapping in cyan, Ti mapping magenta, O mapping in yellow, C mapping in red.

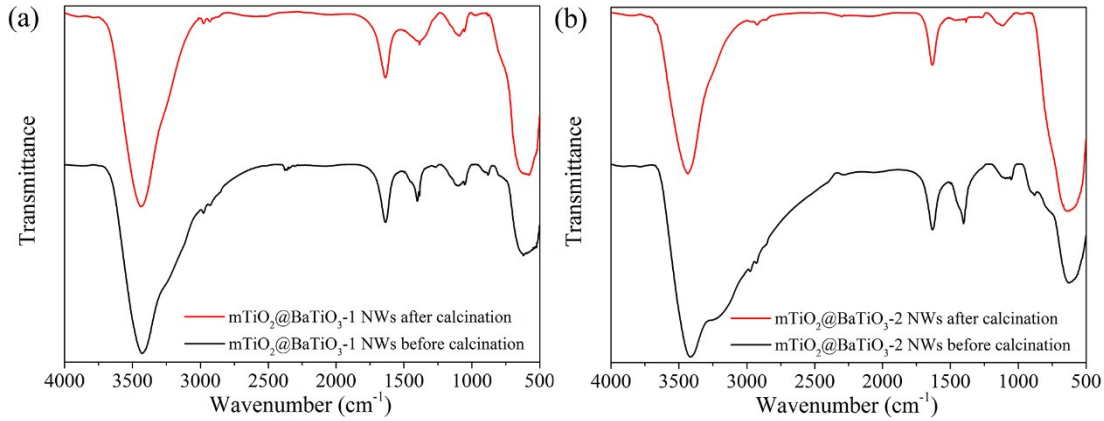

Fig. S4 FT-IR spectra of (a) $mTiO_2$@$BaTiO_3$-1 and (b) $mTiO_2$@$BaTiO_3$-2 NWs before and after calcination.

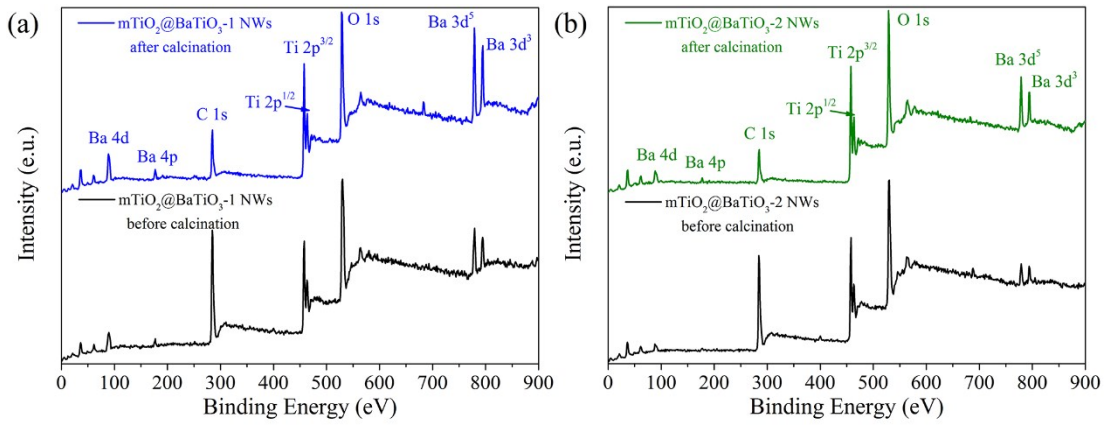

Fig. S5 XPS spectra of (a) $mTiO_2$@$BaTiO_3$-1 and (b) $mTiO_2$@$BaTiO_3$-2 NWs before and after calcination.

Table S1 Survey spectrum quantification of XPS of $mTiO_2$@$BaTiO_3$ and $mTiO_2$@$BaTiO_3$-2 NWs before and after calcination.

composites		species (wt %)			
		Ba 3d	Ti 2p	O 1s	C 1s
$mTiO_2$@$BaTiO_3$-1	before calcination	5.98	6.81	28.66	45.65
	after calcination	15.07	27.83	28.02	29.09
$mTiO_2$@$BaTiO_3$-2	before calcination	2.92	24.79	29.34	42.95
	after calcination	8.86	29.13	30.29	31.72

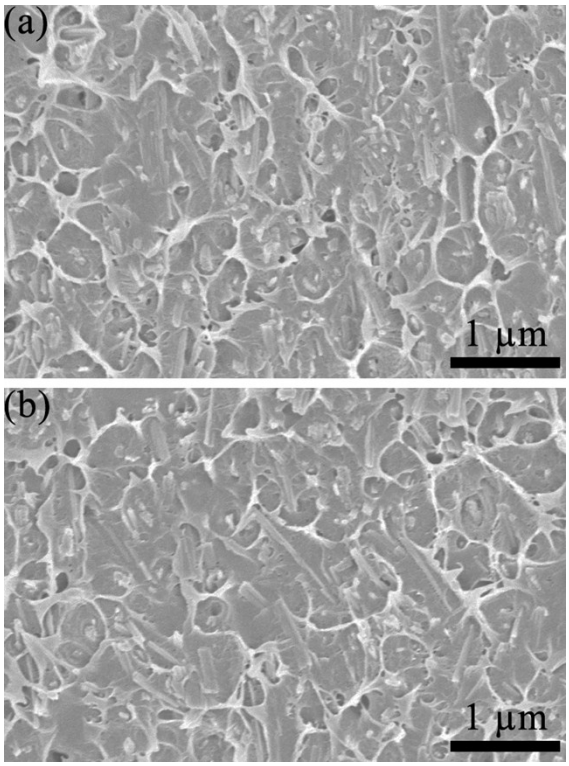

Fig. S6 SEM images of freeze-fractured cross-section surfaces of P(VDF-HFP)-based nanocomposites with 20 wt % loading of (a) $mTiO_2$@$BaTiO_3$-1 and (b) $mTiO_2$@$BaTiO_3$-2 NWs.

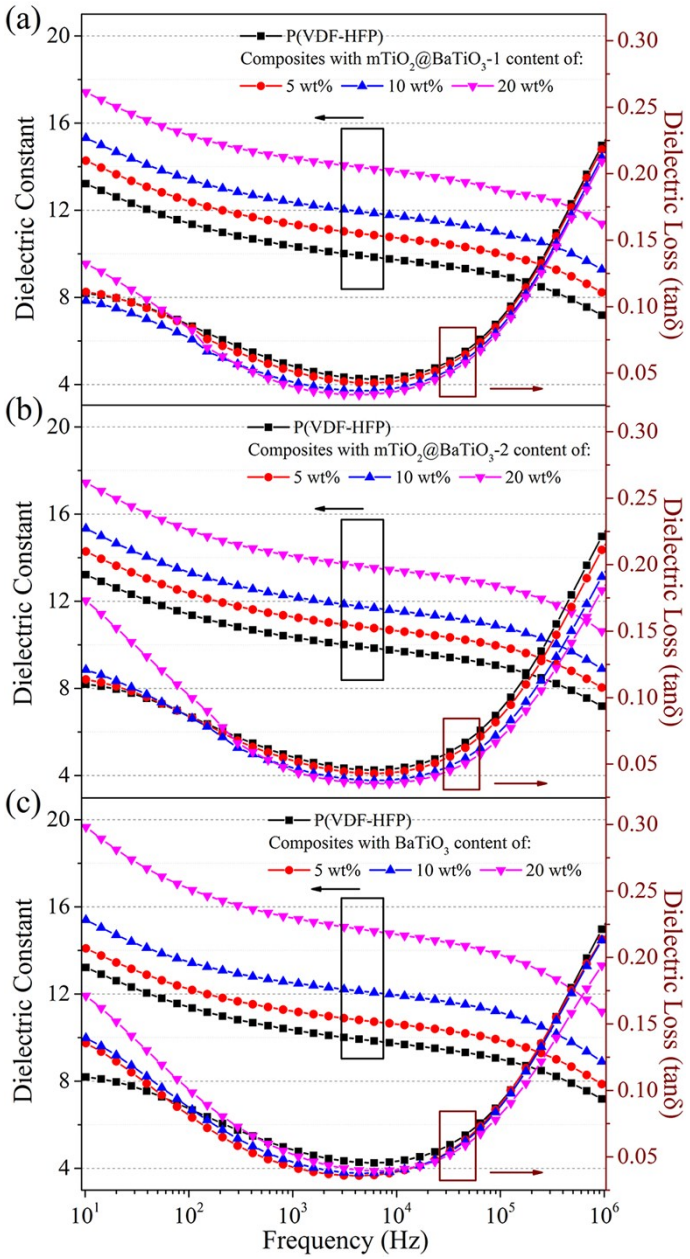

Fig. S7 Dielectric constant and loss spectra for P(VDF-HFP)-based nanocomposites with different weight ratio of (a) $mTiO_2$@$BaTiO_3$-1, (b) $mTiO_2$@$BaTiO_3$-2, and (c) raw $BaTiO_3$ NWs.

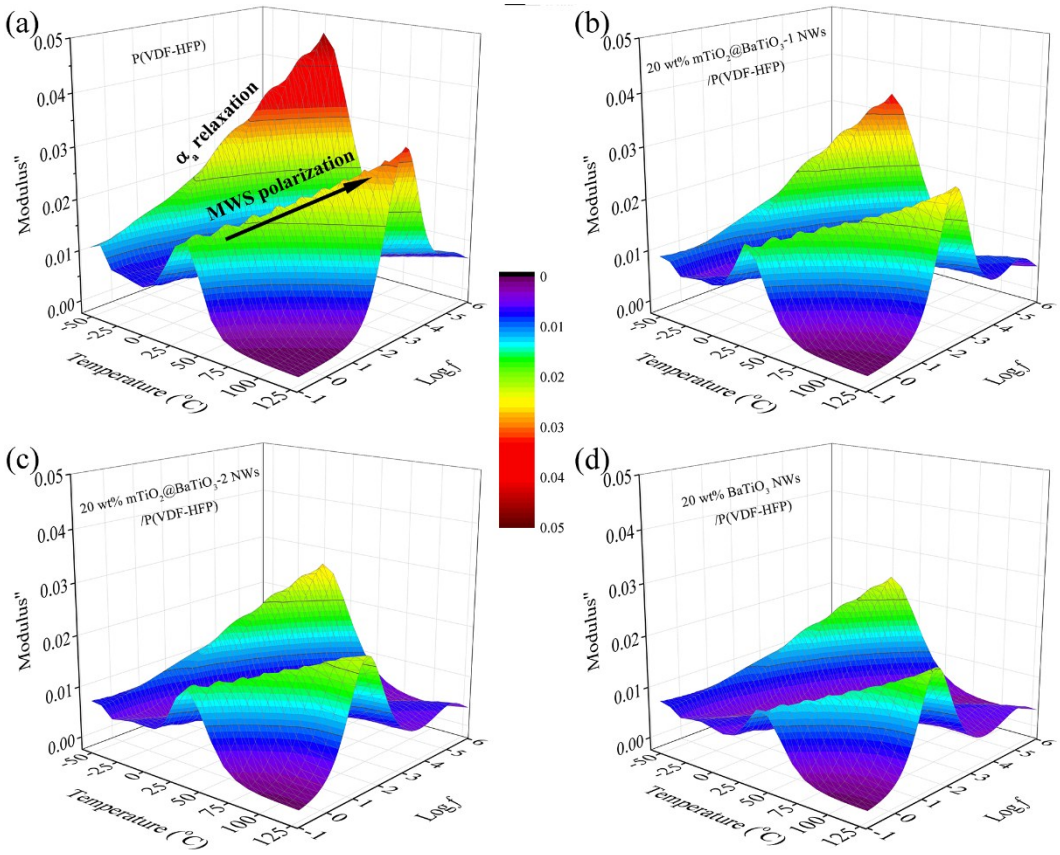

Fig. S8 Frequency dependent of imaginary electric modulus at various temperature of (a) pure P(VDF-HFP) and nanocomposites with 20 wt % of (b) $mTiO_2$@$BaTiO_3$-1, (c) $mTiO_2$@$BaTiO_3$-2, and (d) raw $BaTiO_3$ NWs.

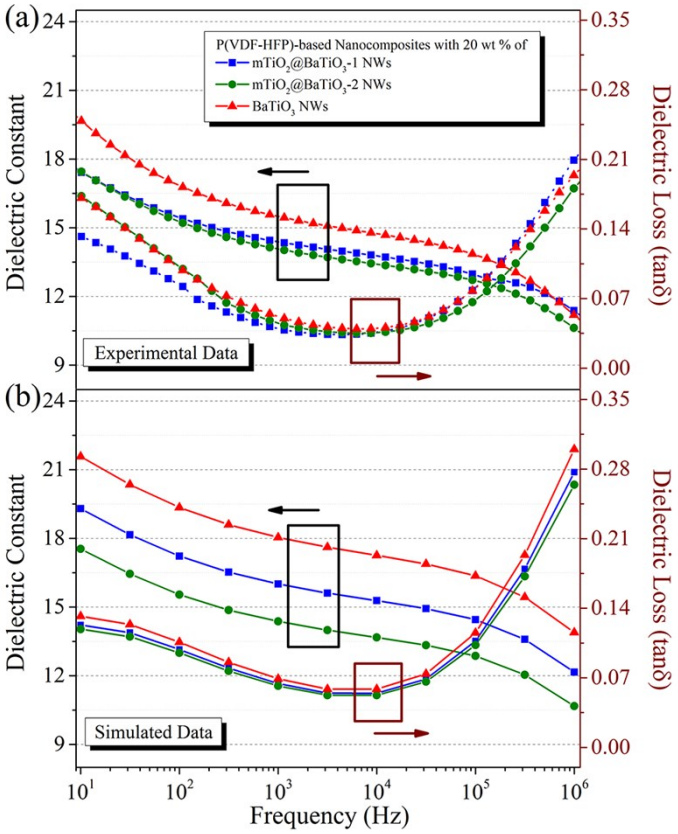

Fig. S9 (a) Experimental and (b) simulated dielectric spectra for P(VDF-HFP)-based nanocomposites with 20 wt % of $mTiO_2$@$BaTiO_3$-1, $mTiO_2$@$BaTiO_3$-2, and raw $BaTiO_3$ NWs.

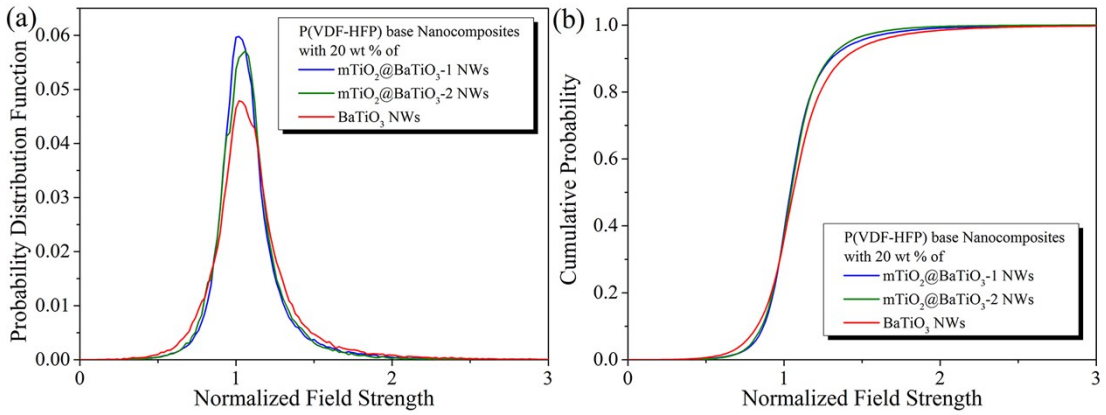

Fig. S10 (a) Probability distrubution function and (b) cumulative probability as a function of normalized filed strength (relative to applied filed).

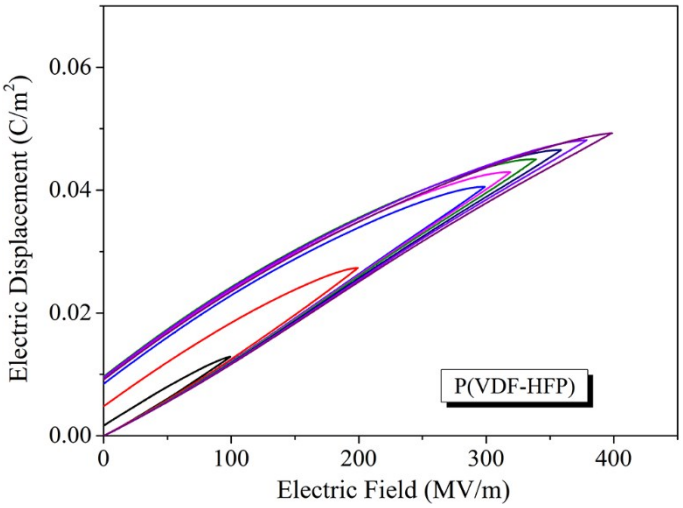

Fig. S11 *D-E* loops under unipolar electric fields of 10 Hz for pure P(VDF-HFP)

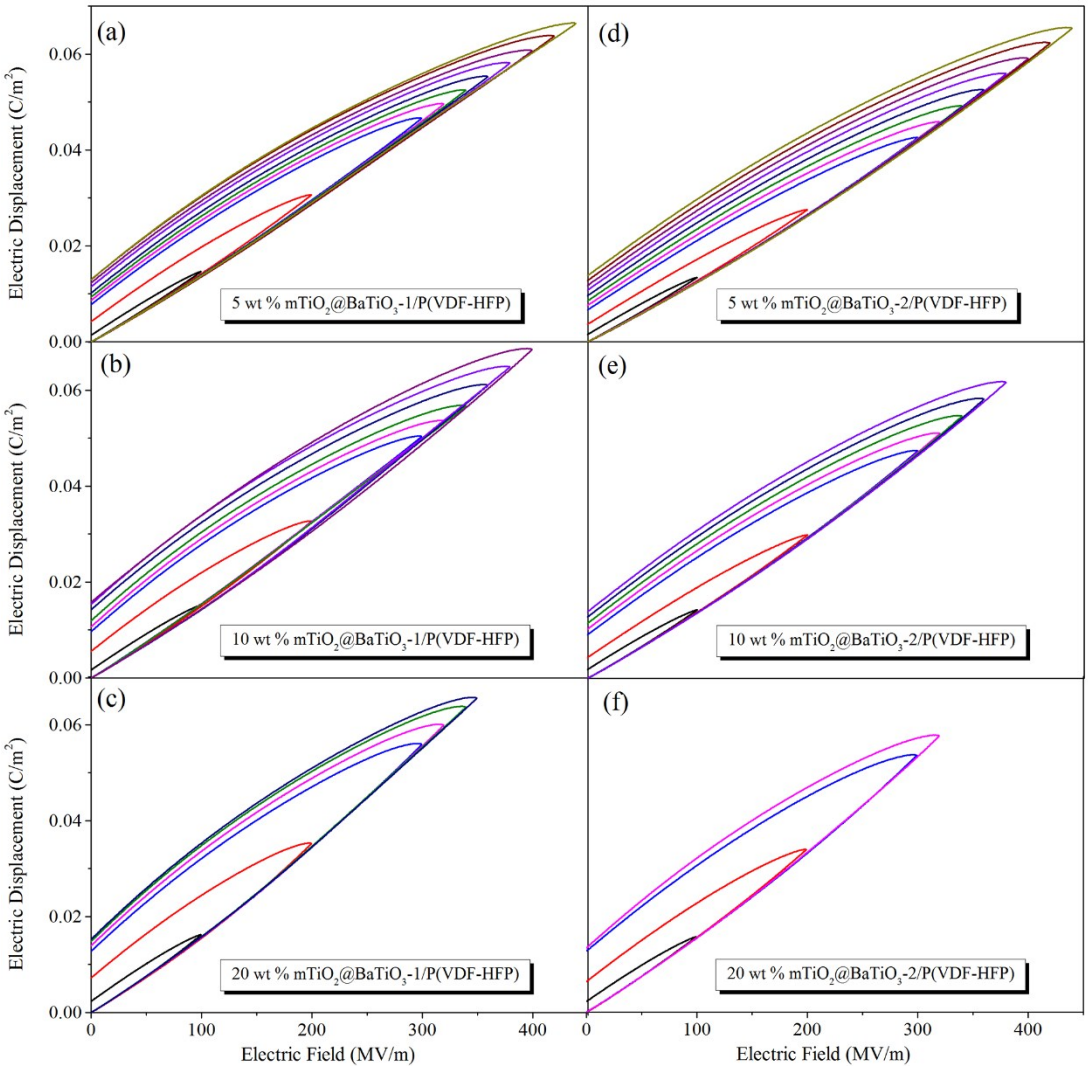

Fig. S12 *D-E* loops under unipolar electric fields of 10 Hz for P(VDF-HFP)-based nanocomposites with (a) 5 wt %, (b) 10 wt %, (c) 20 wt % mTiO$_2$@BaTiO$_3$-1 NWs and (d) 5 wt %, (e) 10 wt %, (f) 20 wt % mTiO$_2$@BaTiO$_3$-2 NWs.

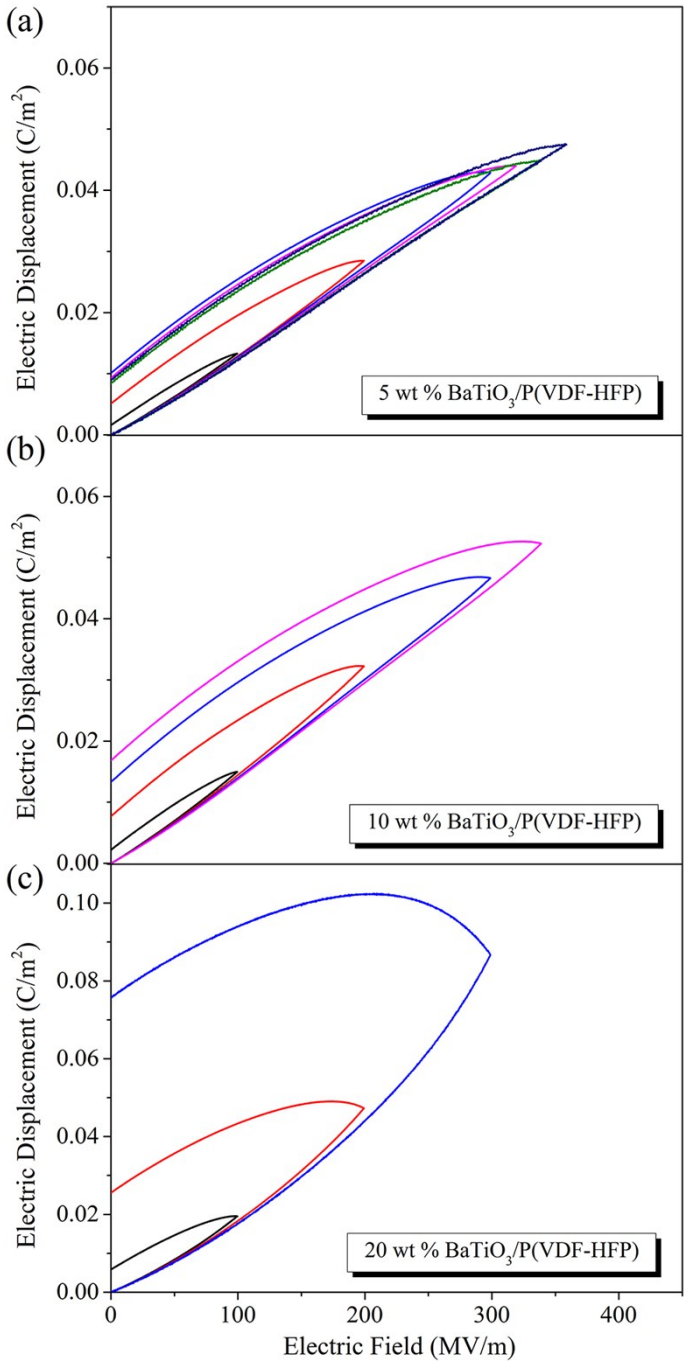

Fig. S13 *D-E* loops under unipolar electric fields of 10 Hz for P(VDF-HFP)-based nanocomposites with (a) 5 wt %, (b) 10 wt %, and (c) 20 wt % raw $BaTiO_3$ NWs.

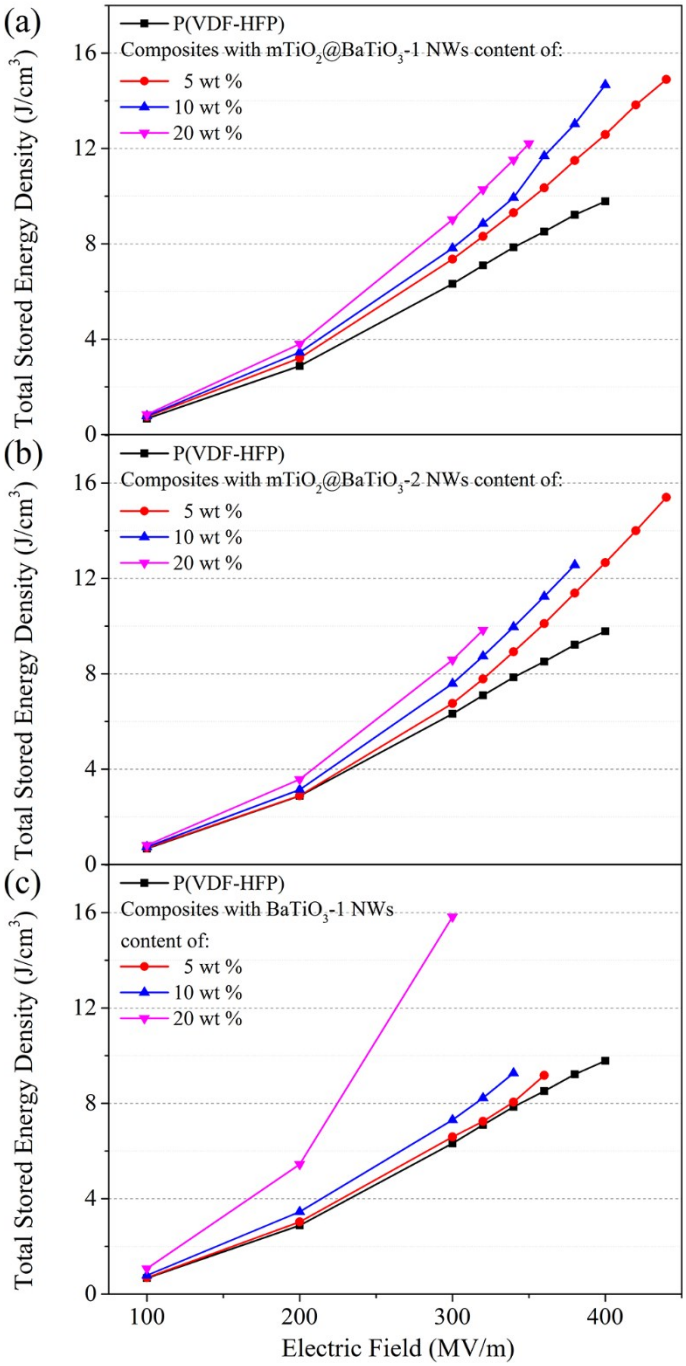

Fig. S14 Total stored energy densities of P(VDF-HFP)-based nanocomposites with different contents of (a) $mTiO_2$@$BaTiO_3$-1, (b) $mTiO_2$@$BaTiO_3$-2 and (c) raw $BaTiO_3$ NWs under varied applied fields.

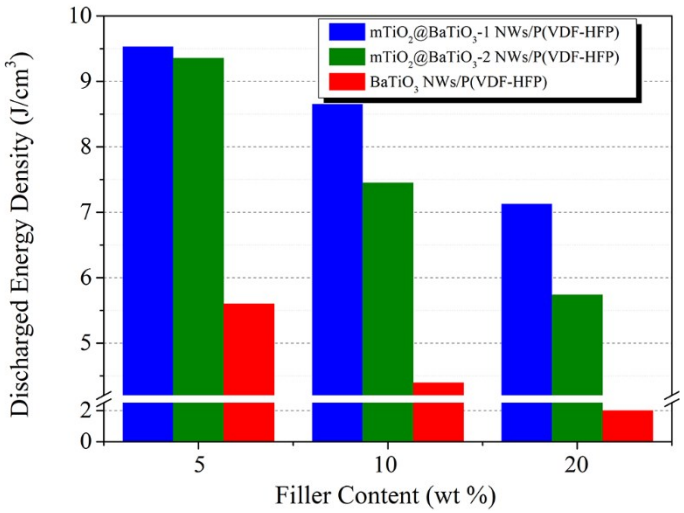

Fig. S15 The maximum discharged energy densities of P(VDF-HFP)-based nanocomposites with different weight fractions of $mTiO_2$@$BaTiO_3$-1, $mTiO_2$@$BaTiO_3$-2 and raw $BaTiO_3$ NWs.